Alternative splicing controls teneurin-3 compact dimer formation for neuronal recognition

Christos Gogou[1], J Wouter Beugelink[2], Cátia P Frias[1], Leanid Kresik[1], Natalia Jaroszynska[3], Uwe Drescher[3,4], Bert J C Janssen[2], Robert Hindges[3,4], and Dimphna H Meijer[1,*]

[1]Department of Bionanoscience, Kavli Institute of Nanoscience Delft, Delft University of Technology, van der Maasweg 9, 2629HZ Delft, the Netherlands

[2]Structural Biochemistry, Bijvoet Centre for Biomolecular Research, Faculty of Science, Utrecht University, Universiteitsweg 99, 3584CG Utrecht, the Netherlands

[3]Centre for Developmental Neurobiology, King's College London, Guy's Campus, London SE1 1UL, UK

[4]MRC Centre for Neurodevelopmental Disorders, King's College London, London SE1 1UL, UK

*Correspondence: Dimphna H Meijer, d.h.m.meijer@tudelft.nl

Keywords: Synaptic cell adhesion, alternative splicing, macromolecular complex formation, single particle cryo-EM, neuronal recognition

Abstract

Neuronal network formation is facilitated by recognition between synaptic cell adhesion molecules (CAMs) at the cell surface. Alternative splicing of CAMs provides additional specificity in forming neuronal connections. For the teneurin family of CAMs, alternative splicing of the EGF-repeats and NHL domain controls protein-protein interactions at the synapse. Here we present a 3.2 Å cryo-EM structure of the compact dimeric ectodomain of teneurin-3 harbouring both splice inserts. This dimer is stabilised by an EGF8-ABD contact between subunits. Cryo-EM reconstructions of all four splice variants, together with SAXS and negative stain EM, reveal compacted dimers for each, with variant-specific dimeric arrangements. This results in specific *trans*-cellular interactions, as tested in cell clustering and stripe assays. The compact conformations provide a structural basis for teneurin homo- and heterophilic interactions. Altogether, our findings demonstrate how alternative splicing results in rearrangements of the dimeric subunits, influencing neuronal recognition and circuit wiring.

Introduction

During the formation of the central nervous system, specific guidance and recognition signals are required to orchestrate the billions of outgrowing neurons as they form complex circuits. Important cues are especially provided by combinations of cell adhesion molecules expressed on the surface of neurons. Among these, teneurins, a conserved family of type II transmembrane proteins, play a crucial role in circuit wiring across various species[1]. However, the molecular mechanisms of how teneurins facilitate the formation of functional neuronal circuits remain poorly understood.

In mammals, there are four family members of teneurins, each expressed in distinct and often interconnected areas of the developing nervous system[2,3]. They have the capability to form homophilic interactions with other teneurins[4–8], as well as heterophilic interactions with other synaptic proteins, enabling a diverse range of functions in circuit development and maintenance[9]. For instance, the interaction between mouse teneurin-3 (Ten3) and latrophilin-2 (Lphn2), an adhesion G-protein coupled receptor (GPCR), orchestrates proper circuit wiring in the hippocampus[7]. This interaction involves a Ten3-Lphn2 repulsive mechanism, where axons expressing Ten3 avoid connecting with Lphn2-expressing target regions. Instead, Ten3-expressing axons grow toward other areas enriched in Ten3, pointing toward homophilic *trans*-synaptic interactions[7,10]. Additional players such as FLRT proteins and Glypican-3 may contribute to ternary complex formation with teneurins to control diverse functions such as neuronal cell migration, synapse formation, and pruning[6,11,12]. Finally, all members of the teneurin family have been associated with diverse neurological disorders[13]. For example, teneurin-1 is linked to autism[14] teneurin-3 to microphthalmia[15], and teneurin-4 to essential tremor[16].

Structural studies of the teneurin ectodomains have revealed a multi-domain ~1850-residue core superfold, prominently featuring a tyrosine-aspartate rich barrel-shaped structure termed YD-shell[17,18]. This YD-shell is adorned with a calcium-binding C-rich domain, a transthyretin-like (TTR) domain and a fibronectin-like region (FN-plug), as well as with a 6-bladed β-propeller NHL domain (NCL-1, HT2A, Lin-41), all located at its N-terminal end[17,18]. At the C-terminal side of the ectodomain, structurally adjacent to the YD-shell, lies an antibiotic-binding domain-like (ABD) fold and a domain akin to the Tox-GGH class of DNases[19]. Connecting the transmembrane helix with the core superfold are a predicted Immunoglobulin (Ig)fold and eight predicted EGF domains (EGF1-8). Notably, EGF2 and EGF5 contain free cysteines that directly contribute to covalent *cis*-dimers formation in all teneurins[20,21]. A homophilic compact *cis*-dimer was resolved for human teneurin-4, which demonstrated a key role for the ABD domain in the dimer interface. In this compact conformation, the ABD domain contacts the C-rich domain, the YD-shell, and the ABD domain of the other subunit. More recently, Li and coworkers reported a *Drosophila* teneurin (Ten-m) homodimer connected through a TTR-NHL interface[22]. This

asymmetric complex was shown to be capable of forming zipper-like higher-order oligomers, most probably as linear superstructures. Two subsequent studies detailed the structural basis of the teneurin-latrophilin interaction. Both works revealed a binding site for the Lec domain of Lphn on the YD-shell of teneurin-2, directly opposite to the ABD and Tox-GHH domains[11,23]. Together, these structural studies unveiled the intricate architecture of teneurin ectodomains, showcasing their multi-domain core superfold and revealing critical insights into their dimeric conformations and interactions, both homo- and heterophilic.

Often, alternative splicing of CAMs plays a crucial role in diversifying their functions and fine-tune cellular interactions. For instance, several synaptic CAMs, such as Dscam, the LAR-RPTP family, neurexin, and neuroligin, harbour few-residue splicing variations that change *trans*-cellular binding sites directly[24–33]. The ectodomains of teneurin proteins also contain two alternatively spliced regions that may combinatorically contribute to the code for molecular recognition at the synapse. The Ten3 splice inserts reside between EGF7 and EGF8 (AHYLDKIVK in mouse Ten3), referred to as splice insert A, and between the first and the second blade of the NHL β-propeller (RNKDFRH in mouse Ten3) referred to as splice insert B. Alternative splicing in teneurins was found to affect binding partner specificity and synaptic differentiation[6,18,23]. For instance, mouse Ten3-A_0B_0, lacking both splice inserts, is not capable of homophilic cell clustering in K562 cells, whereas the presence of either or both splice inserts (A_1B_0, A_0B_1, A_1B_1) was reported to induce clustering in homophilic fashion[10]. Interestingly, Ten3-A_0B_0 (as well as Ten3-A_1B_1, other variants not tested) is capable of inducing heterophilic clusters with latrophilin-3[10].

It is therefore evident that the role of alternative splicing in teneurins is crucial for controlling *trans*-cellular interactions, yet the structural basis of splicing-dependent assembly formation remains unclear. Here, we present a structural comparison of four splice variants of mouse teneurin-3 full ectodomains. Using single particle cryo-electron microscopy (cryo-EM), in combination with small-angle X-ray scattering (SAXS) and negative stain EM, we reveal a novel homo-dimeric interface for teneurin-3 A_1B_1, resulting in a compact dimer conformation. This interface is stabilised by an extended β-sheet interaction between EGF8 and the ABD domain of interacting subunits. Also, A_0B_0, A_0B_1 and A_1B_0 variants are compact dimers in solution, of which only A_1B_0 adopts the same compact conformation as A_1B_1. For the other two variants, an additional contact site is observed between EGF6 and the YD/ABD domains, and each display a different arrangement of the core superfolds. Finally, cell clustering and neuronal stripe assays highlight the capability of the A and B splice insert to directly mitigate *trans*-cellular interactions *in vitro*. Together, these findings support a model wherein the subunits of the Ten3 dimers adopt different orientations due to the presence of relatively small splice inserts. These structural

rearrangements, in turn, expose different binding interfaces that play a crucial role in orchestrating cellular interactions essential for specifying neuronal circuitry formation.

Results

Teneurin-3 A_1B_1 forms a compact dimer through an edge-to-edge-extended β-sheet.

To examine the structural basis of the alternative splice variant A_1B_1 of teneurin-3 (Ten3-A_1B_1), we expressed the complete extracellular domain (ECD, Δ1-341 residues) of N-terminal hexahistidine-tagged mouse Ten3-A_1B_1 in HEK293-E cells (Fig. 1A). We purified the protein by Ni-NTA affinity chromatography followed by size-exclusion chromatography in the presence of calcium (Supplemental Fig. 1A). The purified ECD forms a constitutive dimer, linked by two disulfide bonds in EGF2 and -5 (Cys549 and Cys648, respectively, Fig. 1A). The dimer structure was resolved to 3.3 Å using single particle cryo-electron microscopy, revealing a compact conformation (Fig. 1B, Supplemental Fig. 1D, and Table 1). The core of the compact dimer could be further resolved to 3.2 Å (Supplemental Fig. 1D). In the compact conformation, the NHL domains are facing away from each other (Fig. 1B, middle) and the two subunits are in-plane when viewed from the NHL domain (Fig. 1B, right). The total dimensions of the compact in-plane dimer are 122 Å by 141 Å by 70 Å. The interface is mainly composed of hydrophobic and -phobic surface (Supplemental Fig. 2A).

The main compact dimer interface is formed through an extended edge-to-edge β-sheet between the EGF8 domain (residues 762-764) and the ABD domain (residues 2595-2597) of the two respective subunits (interface I, Fig. 2A, D-E). This interface is only permitted upon displacement of a β-strand on the ABD side, which remains present in a non-compacted subunit reconstruction (Fig. 2C and Supplemental Fig. 2B-D). Residues Gly2576-Ser2582 are observed in the electron density map, and engage in Asp765-Thr2581 and Asn766-Ser2582 hydrogen bonding, but the rest of the loop becomes unstructured (Fig. 2D). Interestingly, a mutation associated with microphthalmia in humans, namely Arg2563Trp[15] in human Ten3 - corresponding to Arg2579 in mouse Ten3 -, is directly flanking the β-strand and participates in the compact dimer interface (Fig. 2C). The EGF8-ABD interface is also supported by hydrophobic interactions between Trp769 and Leu764 on EGF8, and Leu2575 and Val2595 on ABD (Fig. 2D-E). Splice insert A residues Val748-Lys749 are resolved at the N-terminal side of EGF8 (Fig. 2D), and focussed classification of all dimer particles results in extra connected density that folds back onto the ABD domain, which presumably represent the remainder of the insert (Supplemental Fig. 1D). The compact dimer is further stabilised by YD-ABD (interface II, Fig. 2A and F) and YD-YD (interface III, Fig. 2A-B, F-G). Interface III contains between Thr1604-Gly1618 and Thr1607-Asn2589 hydrogen bonding (Fig. 2G). Individually, the interface-contributing residues in EGF8 span a total

interface area (IA) of 462 Å², those in the YD-shell 478 Å², and 629 Å² in the ABD domain (Fig. 2B). Notably, a separate subset of dimer particles harbours no YD-YD interactions, resulting in relatively flexible YD domains hinging at the C-rich/EGF8 region ("open conformation", Supplemental Fig. 1D, Supplemental Videos 1 and 2).

What are the differences between the mouse teneurin-3 compact dimer presented here and the human teneurin-4 (Ten4) compact dimer published previously[5]? The main difference between the Ten3 and Ten4 structures is the orientation of the two subunits with respect to each other (Fig. 3A). The subunits in the human Ten4-A_1B_1 dimer are each turned outwards at a 30° angle, thereby creating a 'transverse dimer' (Fig. 3A). The subunits in the compact dimer configuration of mouse Ten3-A_1B_1, however, align in the same plane (Fig. 1B). In both structures, the ABD domain is central in the interface, but different interactions are formed. In the Ten4 transverse dimer, the ABD domain contacts the C-rich domain, the YD shell and the ABD domain of the other subunit. In the dimer of mouse ten3, the ABD domain contacts EGF8 and the YD shell (Fig. 3B). The difference in dimer conformation results in a molecule with larger dimensions for mouse Ten3 compared to human Ten4 (122 Å by 141 Å by 70 Å versus 133 Å by 166 Å by 112 Å, respectively). A detailed structural comparison reveals that similar residues on the ABD domain and the YD shells are involved in both the transverse versus and in-plane dimer interactions (Fig. 3C). Interestingly, a centrally positioned ABD loop in Ten4 interface - could not be resolved in the in-plane Ten3 compact dimer structure (missing Asn2531-Asn2534, Fig. 2F-G). Altogether, our cryo-EM density map reveals a novel compact conformation of covalently dimerised mouse Ten3, which is different from previously published dimeric conformations of teneurin homologues[5,17,22].

Splice insert A as a potential spacer to dislodge EGF6.

To investigate the effect of splice insert A on the architecture of the EGF-repeat domains, we expressed and purified the full ectodomains and acquired cryo-EM data of all splice variant combinations of mouse Ten3: Ten3-A_0B_0, A_0B_1, A_1B_0 and A_1B_1 (Fig. 4A, Supplemental Fig. 3A-C, and Table 1). Full ectodomain structures of compact dimers could not be resolved, presumable due to air-water interface issues during cryo-EM grid preparation. Similar issues were also observed previously for the Ten4 dimer[5]. Instead, we resolved non-compacted subunits containing partial EGF-repeat domains for each of the proteins (Fig. 4B and Supplemental Fig.3D). Comparison of the four structures reveals that the subunits adopt similar conformations with largest differences in the orientation of EGF6 and EGF7. In absence of splice insert A (A_0B_0 and A_1B_1 isoforms), EGF-repeats 6-8 run across the FN domain towards the YD shell, whereby

EGF6 is located in a groove between the YD shell and ABD domain of the same subunit (Fig 4C). EGF6 directly contacts several negatively charged aspartic acids on the YD β-barrel (Fig. 4C), and Gln2522 in the ABD domain. However, in the presence of splice insert A (A_1B_0 and A_1B_1 isoforms) – predicted to be a 9-residue helix inserted in the linker between EGF7-8 -, EGF6 and EGF7 cannot be resolved anymore, suggesting increased flexibility of EGF6 with respect to the YD shell. Possibly this splice insert acts as a physical spacer to dislodge EGF6 out of its binding groove, hereby preventing the EGF6-YD/ABD interface to form. Low-resolution EM density of the potential splice insert A can indeed be observed hovering over the ABD domain (Supplemental Fig. 1D), thus dislodging EGF6 from its YD/ABD groove. The increased rigidity of EGF6 and EGF7 with respect to the YD shell in the absence of splice insert A appears to hinder EGF8 from interacting with the ABD domain on the other subunit (Fig. 4D-E) - an interaction necessary for the compact dimerization observed in A_1B_1 (Fig. 2C-E). Thus, depending on splice insert A, the EGF-repeat region reorganises relative to the core superfolds, with potential implications for the orientation of the two subunits themselves, and further homo- or heterodimeric interactions.

All isoforms are compact in solution in a calcium-dependent manner.

To further investigate the splicing-dependent effects on the conformation of the Ten3 dimers in solution, we performed small-angle X-ray scattering (SAXS). In presence of calcium, all isoforms are compact in solution (Fig. 5A), with average radii of gyration (Rg) 7.3, 7.8, 7.7, and 7.9 nm, for Ten3-A_0B_0, A_0B_1, A_1B_0, and A_1B_1, respectively (Fig. 5A and Supplemental Fig. 5B). The absence of calcium, as well as the addition of calcium chelator EDTA, result in increased radii of gyration for all isoforms (Fig. 5A and Supplemental Fig. 4B), as well as a loss of the distinct compact-protein profile in the dimensionless Kratky plot (Supplemental Fig. 4A). These effects are similar to the transition of Ten4 from a compact conformation into a more elongated conformation in the absence of calcium[5]. Notably, in the presence of calcium, out of the four splice variants A_0B_0 is most compact in the presence of calcium, whereas A_0B_1 deviates most from a compact form (Fig. 5A). The increased compactness of A_0B_0 could possibly be explained by a predicted interaction between any of the flexible Ig or EGF domains and the splice site B within the NHL domain, that would condense the A_0B_0 compact dimer even further (Supplemental Fig. 6). The data further show that Ten3-A_1B_0 and A_1B_1 have highly similar SAXS profiles. Thus, it appears that splice insert B affects compact dimerization only in absence of splice insert A. The general compactness in presence of calcium is supported by increased protein stability observed as a thermal shift in the protein melting curves of all splice variants (Fig. 5B and Supplemental Fig. 4C). Note that calcium-binding

residues of the C-rich domain of human Ten4 are well-conserved in mouse Ten3 (Fig. 3C), suggesting that the C-rich domain of Ten3 also selectively binds calcium ions.

To corroborate the SAXS profiles indicating compact conformations for all splice variants, we collected negative stain TEM (nsTEM) datasets for all variants. The 2D classifications of all Ten3 splice variants indeed revealed compact conformations for each variant (Fig. 5C). Whereas Ten3-A_1B_0 and A_1B_1 have conformations similar to the cryo-EM structure of A_1B_1, A_0B_0 and A_0B_1 revealed alternative architectures. While the low resolution of the data precludes detailed analysis, a potential YD-YD interface is observed for A_0B_0 – also observed at low abundance in cryo-EM 2D classes (Supplemental Fig. 4E) -, and the A_0B_1 compact dimer could be explained by an FN-FN interaction. 3D reconstructions and low-resolution fitting confirmed these potential dimer interfaces (Fig. 5D). Splice site B is not directly involved in any of the observed compact dimer interfaces, hinting at an unresolved allosteric mechanism that could explain the shifts between A_0B_0 and A_0B_1 conformations. Notably, an additional dimer interface was observed in the negative stain TEM dataset of the A_0B_0 variant, in which the NHL domains are connected (Supplemental Fig. 4F). This conformation would, however, not be compatible with a compact dimer due to restraints imposed by the EGF2-2/5-5 disulfide bond, and may represent an additional higher-order *cis* contact.

We next used the SAXS profiles and compact dimer interfaces from nsTEM to model the structures of the full ectodomain of all the splice variants (Supplemental Fig. 4G). For SAXS modelling, the dimer interfaces obtained from nsTEM were restrained, whereas the domains in the EGF-Ig stalk were treated as independent connected rigid bodies, with EGF2-4 restrained to enforce the intermolecular disulfide bonds. All modelled splice variants, except for the A_0B_1 dimer, explain their SAXS profiles well (Supplemental Fig. 4G). Possibly, the SAXS data of A_0B_1 cannot be explained by the nsTEM-based model, because A_0B_1 in solution does not exhibit the same level of compactness or adopts multiple conformations. Nonetheless, the combination of the nsTEM and SAXS data indicates at least three different dimer conformations, with A_1B_0 and A_1B_1 sharing the same EGF8-ABD mediated dimer, also observed in the A_1B_1 dimer cryo-EM structure, and splice variants A_0B_0 and A_0B_1 each adopting a distinct dimer conformation.

A model for splice-dependent *trans*-interactions.

The alternative conformations as shown in Fig. 5 may affect the capabilities of Ten3 splice variants for *trans*-cellular interactions. To test this, we electroporated GFP-tagged full-length transmembrane variants of all four Ten3 splice variants in K562 hematopoietic cells. *Trans*-cellular

interactions were quantified by assessing cluster formation of the Ten3 electroporated K562 cells (Fig. 6A-B and Supplemental Fig. 5A). Similar to previously shown[10], all isoforms except A_0B_0 form homophilic clusters. In addition, we observe a quantitative difference between clustering of Ten3-A_0B_1, A_1B_0 and A_1B_1, whereby A_1B_0 and A_1B_1 have only limited clustering capabilities, while electroporation with A_0B_1 results in the highest clustering index and cluster size averages (Fig. 6B). As such, similar to the structural data (Fig. 5), splice insert B has a large effect, but exclusively when splice insert A is absent.

No *trans*-interaction is observed in the cell clustering assay for Ten3-A_0B_0 (Fig. 6C). Possibly, the A_0B_0 may not engage in *trans*-cellular interactions because it forms homophilic complexes in *cis*, through the above-mentioend NHL-NHL contact (Supplemental Fig. 4F). To model higher-order interactions that may explain the observed *trans*-cellular interactions for the other variants, we analysed dimer-of-dimer formation of the SAXS- and nsTEM-based full ectodomain models. For compact dimer Ten3-A_0B_1, harbouring a potential FN-FN interface, the ABD domain would be accessible to form a *trans* dimer-of-dimer interaction with the EGF8 domain of a dimer at the opposing membrane (Fig. 6C). This interface could not be employed for dimer of dimers in *cis* due to increased constraints induced by the EGF6-ABD/YD interaction. Remarkably, the A_0B_1 *trans* dimer-of-dimers displays an additional NHL-NHL interface between them (close-up, Fig. 6C), with splice inserts B located at this interface. This interface is reminiscent of the teneurin-2 crystal contact reported previously[17]. Compact dimers A_1B_0 and A_1B_1 could form *trans*-cellular interactions by means of the FN-FN interface (Fig. 6C). This same interface could also be employed for an additional *cis*-interaction (Fig. 6C). A presumed equilibrium between *cis*- and *trans* dimers of dimers would explain the limited cell-clustering capability of the A_1B_0 and A_1B_1 dimers, as *cis* dimers-of-dimers would harbour no potential for *trans*-interactions. The distinct conformations of compact dimers may also have implications for their ability to bind *trans*-cellularly with latrophilin. As illustrated in Supplemental Fig. 5B, A_0B_1 may not readily engage in *trans*-interaction with latrophilin, given that the latrophilin-interaction surface appears to be oriented towards the membrane, obstructing access to the Olfactomedin-Lectin domain. The other three splice variants seem to be more conducive to latrophilin binding. This observation aligns with earlier findings that indicated the exclusive incapability of a teneurin-2 A_0B_1 version to bind latrophilin, and thus provides a structural basis for the proposed shapeshifting mechanism[7,10,23].

Splice insert B attracts outgrowing axons of teneurin-3-expressing neuronal explants.

We hypothesised that the emergent NHL-NHL contact in Ten3-A_0B_1 (close-up Fig. 6C) could provide additional *trans*-cellular stabilisation in a B-dependent manner. To address this hypothesis and whether this contact by itself provides sufficient adhesive strength, we set up chick retinal stripe assays. First, we characterised Ten3 expression patterns in the chick retina, using RNA fluorescent *in-situ* hybridization (FISH). We observed that Ten3 mRNA is highly expressed in the ventral, but not dorsal, retina. (Fig. 7A). Then, to address whether Ten3 acts as an attractant or repellent for neurons from either retinal regions, we plated retinal chick explants from both regions and grew them on Ten3 stripe assays. To directly evaluate the impact of splice insert B on *trans*-cellular interactions, we utilised a monomeric variant of mouse Ten3 lacking the Ig and EGF domains (residues Δ1-845). This specific monomer is incapable of establishing EGF8-ABD interactions, shown in this work to restrict the influence of splice insert B. Furthermore, the designed Ten3 monomeric variant cannot participate in the A_0B_1 EGF8-ABD-based dimers-of-dimers *trans*-interaction, thereby isolating the contribution of B in direct *trans*-cellular binding. At 2-3 days after explant growth, it was observed, that ventral neurons localised preferentially to the Ten3-B_1-covered regions with their axons growing parallel to the stripes, whereas the dorsal neurons covered the entire surface with axons growing in random directions (Fig. 7B-D). No such difference was observed when culturing ventral or dorsal neurons on Ten3-B_0 stripes (Fig. 7E-F). Notably, when only labelled and unlabelled control antibody was immobilised in the stripe assay, neither the ventral nor the dorsal neurons showed any preferential growth over particular stripes. (Fig. 7C-F). The K562 and retinal explant studies together show that, while the presence of splice insert A may allow for *trans*-cellular clustering in a manner unaffected by B, the presence of splice insert B itself can support and induce robust *trans*-cellular interactions and serves as an attractant to chick retinal neurons from the ventral region.

Discussion

Cell adhesion molecules (CAMs) play a prominent role in the process of neuronal wiring by establishing a molecular recognition code at the synapse through their combinatorial expression pattern. Teneurins are a family of synaptic CAMs that exhibit additional *trans*-synaptic specificity through alternative splicing of two inserts, referred to as splice insert A and splice insert B. Here, we reveal a compact dimer conformation of the ectodomain of mouse Ten3-A_1B_1. The compact dimer interface is formed through an extended β-sheet interaction between the EGF8 and ABD domains on interacting monomers. Additionally, the YD-shell and ABD domain participate in further stabilisation. We resolved the cryo-EM subunits of each splice variant, and these data demonstrate an additional interaction between EGF6 and the ABD/YD domain, only when splice insert A is absent. We further provide small-angle X-ray

scattering (SAXS)-based evidence, complemented with negative stain EM, that all splicing variants are compact in presence of calcium. Splice variant A_1B_0 adopts a similar conformation as A_1B_1 while A_0B_0 and A_0B_1 display different compact conformations. These large rearrangements of the two subunits have practical implications for *trans*-cellular interactions, as demonstrated in the hematopoietic cell line K562 and chick retinal neurons. Our data provide a model where relatively short splice inserts of ~7 amino acids result in large structural rearrangements, hereby impacting *trans*-cellular interactions and neural circuit wiring.

Trans-synaptic adhesion is commonly regulated by alternatively splice variants, often directly affecting the *trans*-cellular contacts[10,34–37]. For instance, the neuroligin-neurexin complex is regulated by the presence of two neuroligin splice inserts (A, 30 residues; B, 8 residues) that directly occlude neurexin binding[31]. Wilson and colleagues further revealed that the presence of a neurexin splice insert (2A, 8 residues) elongates a β-sheet near the interface with neurexophilin, directly stabilising this complex[32]. Similarly, two 'micro-exons' A and B (meA, 9 residues; meB, 4 residues) strongly determine *trans*-synaptic binding for PTPδ, PTPσ, and LAR, three members of the LAR-RPTP family[37]. The inserts were shown to either directly remodel the *trans*-synaptic interface[24–32], or - in the case of meB as a linker between Ig2 and Ig3 - by increasing the flexibility of Ig3 relative to Ig1/Ig2[33], thereby extending the interface. These inserts then determine selective binding of PTPδ to IL1RAPL1 and IL-1RAcP[33], Slitrk1/2[28,29], and SALM5[30], and the interactions of PTPσ with SALM3[38] and TrkC[39a]. Similarly, cell-specific expression of Dscam splice variants – with a total of 38,016 possible Dscam isoforms - underlies dendritic self-avoidance[40], and various structural works have shown how Dscam splicing directly remodels the homophilic binding interface to orchestrate different *cis* and *trans* interactions[24–27]. These findings are all examples in which the *trans*-cellular binding interface is directly modulated by small splice variations.

In contrast, our data illustrate how alternative splicing of teneurin-3 results in large rearrangements of the individual subunits, referred to as shapeshifting by Li et al[23], forming different compacted dimers, and thereby exposing new binding sites. Specifically, the presence of splice insert A increases the flexibility of the EGF repeat region, thereby facilitating EGF8-ABD compact dimers to form. Additionally, the presence of splice insert B facilitates an FN-FN compact dimer, - but only in absence of splice insert A. Our data does not explain why Ten3-A_0B_0 and Ten3-A_0B_1 are structurally different. Although splice insert B locally only modifies the loop in which it is located (Supplemental Fig. 6A), we speculate that the NHL domain (including splice site B) may be engaged in a direct contact with any of the Ig or EGF domains (Supplemental Fig. 6B-D). This would impose or remove additional restraints resulting in FN-FN compact dimers for the Ten3-A_0B_1 variant (Supplemental Figure 6).

Importantly, these different compact dimer conformations expose different surfaces available for dimer-of-dimer formations in *trans*. For instance, the EGF8-ABD compacted dimers are exposing FN domains for FN-FN *trans* interactions. Conversely, the FN-FN compact dimers are exposing the EGF8 and ABD domains for *trans* and *cis* dimers-of-dimers.

In recent years, it has become evident that the pre- and postsynaptic membranes are tightly organised[41]. For instance, post-synaptic receptors are aligned with pre-synaptic vesicle release sites, hereby forming nanodomains, and potentially enhancing the efficiency of signal transfer. Cell adhesion molecules may also play a significant role in this process by directly interacting with receptors to orchestrate the molecular organization at the synaptic membrane. Indeed, few studies have now shown that cell adhesion molecules are also present in nanodomains, exemplified by neurexins[42]. More recently, using STORM super-resolution microscopy, researchers discovered that teneurin-3 is also organised in nano-size clusters, of approximately 80 nm in size, localised at the pre-synaptic side[43]. It would be interesting to explore further what is required to form such 80 nm clusters, as our *cis*- and *trans*-interactions only resulted in linear arrays (data not shown). This outcome resembles what is predicted from the asymmetric dimeric contact observed in fly teneurin[22]. Presumably, formation of such clusters may require the presence of additional cell adhesion molecules, membrane-embedded proteins, lipids, or interacting receptors.

Taken together, an underlying principle is emerging regarding the relationship between alternative splicing and neural connectivity. Teneurin's splicing-dependent conformational reorganisations itself present a unique example of large rearrangements causing indirect remodelling of *trans*-synaptic interactions. These splicing-dependent conformation acrobatics shed light on how small changes in protein sequence realise large conformational shifts at the molecular level, and orchestrate neuronal circuitry formation up to the scale of entire nervous systems. Future studies will have to address the cell-specific expression of such splice variants and the consequences for neuronal wiring specificity.

Data Availability

Cryo-EM data have been deposited to the PDB and EMDB databases, with the following identifiers: PDB ID 8R50, PDB ID 8R51, PDB ID 8R54, EMD-18889, EMD-18890, EMD-18891, EMD-18900, EMD-18902. See Table 1 and Supplemental Figure 1D for specifications. SAXS data have been deposited to the SASBDB databases and assigned the identifiers: SASDTY2, SASDTZ2, SASDT23, SASDT33,

SASDT43, SASDT53, SASDT63, SASDT73, SASDT83, SASDT93, SASDTA3, SASDTB3, SASDTC3, SASDTD3, SASDTE3, SASDTF3, SASDTG3, SASDTH3, SASDTJ3.

Acknowledgements

Cryo-EM data were collected at The Netherlands Centre for Electron Nanoscopy (NeCEN) with assistance from Willem Noteborn. We acknowledge the European Synchrotron Radiation Facility (ESRF) for provision of synchrotron radiation facilities and we would like to thank Petra Pernot for assistance and support in using beamline B29. B.J.C.J. is supported by an NWO grant (OCENW.KLEIN.026). D.H.M. is supported by an NWO computing grant (2021.058) and NWO Veni grant (722.016.004),

Author contributions

Conceptualization: CG, DHM

Methodology: CG, JWB, CPF, NJ, UD

Data acquisition and analysis: CG, JWB, CPF, NJ, LK

Supervision: RH, BJCJ, DHM

Writing – original draft: CG, JWB, CPF, BJCJ, RH, DHM

Writing – review & editing: CG, JWB, CPF, NJ, LK, BJCJ, RH, DHM

Declaration of interests

The authors declare that they have no known competing financial interests or personal relationships that could have appeared to influence the work reported in this paper.

Inclusion and diversity statement

In line with our commitment to promoting a diverse and inclusive scientific community, we affirm our dedication to upholding the principles of equity and diversity in the research presented in this paper. We believe that diversity in the scientific community is essential to drive innovation, foster creativity, and ensure comprehensive and unbiased exploration of the life sciences.

Tables

Table 1: Cryo-EM data collection and refinement statistics.

Data collection and processing	Teneurin-3 A_1B_1 Compact dimer	Teneurin-3 A_1B_1 Subunit	Teneurin-3 A_0B_0 Subunit	Teneurin-3 A_0B_1 Subunit (EGFs focused)	Teneurin-3 A_1B_0 Subunit (EGFs focused)
Magnification	105,000x	105,000x	105,000x	105,000x	105,000x
Electron exposure ($e^-/Å^2$)	50	50	50	50	50
Voltage (kV)	300	300	300	300	300
Defocus range (μm)	-0.8 to -2.0	-0.8 to -2.0	-0.8 to -2.3	-0.8 to -2.0	-0.8 to -2.0
Pixel size (Å)	0.836	0.836	0.836	0.836	0.836
Symmetry imposed	C2	C1	C1	C1	C1
Initial particle images (n)	2,904,462	2,904,462	2,182,558	1,197,761	1,005,254
Final particle images (n)	36,680	69,290	66,637	67,787	47,915
Map resolution (Å)	3.3	3.2	3.5	3.2	3.4
FSC threshold	0.143	0.143	0.143	0.143	0.143
Map resolution range (Å)	3.2-4.9	3.1-4.5	3.4-4.8	3.2-5.4	3.2-6.2
Refinement					
Initial model used (PDB code)	6FAY	6FAY	6FAY		
Model resolution (Å)	3.5	3.2	3.6		
FSC threshold	0.5	0.5	0.5		
Model composition	EGF8 through Tox-GHH	EGF8 through Tox-GHH	EGF6 through Tox-GHH		
Non-hydrogen atoms	29,762	13,977	15,898		
Protein residues	3,782	1,793	1,982		
Ligands (glycans)	32	13	24		
B factors ($Å^2$)					
Protein	58.38	37.02	87.02		
Ligand	66.77	40.61	99.70		
R.m.s. deviations					
Bond lengths (Å)	0.002	0.004	0.004		
Bond angles (°)	0.431	0.505	0.572		
Validation					
MolProbity score	1.88	1.76	2.00		

Clash score	7.92	6.60	8.97		
Poor rotamers (%)	0.00	0.35	0.35		
Ramachandran plot					
Favoured (%)	92.89	94.14	90.94		
Allowed (%)	7.06	5.86	8.91		
Disallowed (%)	0.05	0.00	0.15		

Methods

Plasmids

The ectodomain and full-length version of Ten3-A_0B_0 (MGC premier cDNA clone BC145284, Biocat GmbH, BamH1 sites removed with silent mutations) were cloned into the pUPE106.03 and pUPE3820 vectors (U-protein Express), containing a N-terminal cystatin secretion signal followed by a hexa-His tag or a N-terminal GFP tag, respectively, by using BamHI and NotI restriction sites. Ectodomains and full-length splice variants of Ten3-A_0B_1, Ten3-A_1B_0, Ten3-A_1B_1 were constructed from full-length Ten3-A_1B_1 using PmlI-AgeI, EcoRI-PmlI and EcoRI-AgeI restriction ligation cloning. Monomeric mouse Ten3 (residues 846–2715) for stripe assays as in Jackson et al. 2018[17].

Protein expression and purification

Epstein–Barr virus nuclear antigen I-expressing HEK293 cells (HEK-E; U-Protein Express) were used to express all secreted Ten3 ECD isoforms. Cells were cultured in FreeStyle293 expression medium with GlutaMAX (FreeStyle; Gibco) supplemented with 0.2% fetal bovine serum (FBS, Gibco) and 0.1% Geneticin (G418 Sulfate; Gibco), in a shaking incubator at 37 °C and 5% CO_2. Prior to transfection, HEK-E cells were seeded at 0.25-0.32 x 10^6 cells/mL onto 1L Erlenmeyer cell culture flasks in FreeStyle medium without supplements.24h later, cells were transfected with a total of 125 μg DNA encoding the full ECD per 250 mL of cells using polyethylenimine (PEI, 1:3 DNA:PEI ratio; Polysciences), according to the manufacturer's protocol, and treated with 5.5% Primatone in Freestyle medium 6-24h post-transfection. Six days after transfection, the medium was collected by pelleting the cells through centrifugation at 300g for 10 min. The medium was once again centrifuged at 4000g for 10 min to remove any remaining cells from the medium. Proteins were purified by Ni-NTA affinity chromatography using an elution buffer containing 25 mM HEPES (pH 7.8), 500 mM NaCl, and 500 mM Imidazole, followed by size-exclusion chromatography (SEC) using a Superose6 Increase 10/300 GL column (Cytiva) into a final buffer composition (SEC-buffer) of 20 mM HEPES (pH 7.8), 150 mM NaCl. After each Ni-NTA

affinity and SEC purification step, the proteins were concentrated using a 15 mL Amicon ultra centrifugal filter at 100 kDa cut-off. The final SEC-buffer was either supplemented with 2 mM $CaCl_2$ or concentrated proteins were dialysed overnight at 4 °C using 3.5K MWCO Slide-A-Lyzer MINI Dialysis Devices (Thermo Scientific) in 100 mL SEC buffer containing 2 mM $CaCl_2$. Purified proteins were diluted to 20 µg/mL, boiled for 5 min at 98 °C in the presence or absence of β-mercaptoethanol and loaded onto a TGX mini protean precast gel (Biorad) for 50 min at 200V.

SEC-MALS

The oligomeric and conformational states of the different purified isoforms were probed and directly compared by using analytical size exclusion chromatography with subsequent multi-angle light scattering (SEC-MALS). The Ten3 isoforms, along with a bovine serum albumin (BSA) reference, were diluted to a final concentration of 0.5 mg/mL in SEC buffer (20 mM HEPES pH 7.8, 150 mM NaCl.) supplemented with 2 mM $CaCl_2$ and loaded onto a Superose6 Increase 10/300 GL column (GE Healthcare) integrated on a high-performance liquid chromatography (HPLC) unit (1260 Infinity II, Agilent) with an online UV detector (1260 Infinity II VWD, Agilent), an 8-angle static light scattering detector (DAWN HELEOS 8+, Wyatt Technology), and a refractometer (Optilab T-rEX, Wyatt Technology) in series. On the basis of the measured Rayleigh scattering at different angles and the established differential refractive index increment of value of 0.185 $ml \cdot g^{-1}$ for proteins in solution with respect to the change in protein concentration (dn/dc), weight-averaged molar masses for each species were calculated using ASTRA software (Wyatt Technology; v.7.3.1).

Cryo-electron microscopy and data processing

All cryo-EM imaging of Ten3 ECDs was performed on purified protein samples diluted in SEC-buffer supplemented with 2mM $CaCl_2$ to a final concentration of 0.5 mg/mL. 3.0µL of diluted sample was deposited onto Quantifoil R1.2/1.3 Cu 300 mesh grids that were glow-discharged for 1 minute at 15mA. Excess sample volume was blotted away for 2.5-4.0 seconds with blot force of -3.0 at 22°C and 100% humidity before plunging into liquid ethane using a Vitrobot Mark IV (Thermo Scientific). Movies were acquired using a K3 detector (Gatan) in counting super-resolution mode with a 20keV (Gatan) slit width at 105,000x nominal magnification, a corresponding super-resolution pixel size of 0.418Å, and a total dose of 50 $e^-/Å^2$ per movie. A total of 10,927; 3,888; 4,412 and 8,447 movies were acquired for the A_0B_0, A_0B_1, A_1B_0, and A1B1 isoforms, respectively, at a defocus range of -0.8 to -2.0 µm (-0.8 to -2.3 µm for the A1B1 isoform). All datasets were processed using RELION3.1[44] unless otherwise stated. Beam-induced motion and drift correction was performed using MotionCorr2[45] with a pixel binning factor of 2 (0.836Å physical pixel size), and Ctf estimation by using Gctf[46]. Particles were initially picked from the

corrected images using RELION's own Laplacian-of-Gaussian method, upon which a manual selection from subsequent 2D classification was used for reference-based particle re-picking. 2D classification was used to clean data of non-particle objects like foil hole edges and ice crystals from the extracted particle sets. Random subsets of particles were further 2D classified to select class averages for *ab initio* reconstruction of a reference for 3D classification on the full set of particles that were cleaned through 2D classification. For all datasets, 3D map reconstructions were performed according to the regular workflows of Relion3.1, and as reported in the corresponding supplemental figures. C2-to-C1 symmetry expansions for the A1B1 compact dimer were performed on refined particle datasets. Particle subtraction was performed without automated centering of the resulting maps. For particle subtraction in symmetry-expanded data, the C2-to-C1 particles were first refined with a full-map reference in C1 before masking regions of interest on a single subunit for subtraction outside the masked region. To select particles within datasets that contained good-quality signal for the EGF domains and splice insert A, focussed 3D classification was performed with increased regularization parameters T, while masking the region of interest. To visualize the compact dimer movement from open to closed conformation, 3D variability analysis in CryoSPARC[47] was used. CryoSPARC's local refinement was used for reconstruction of the dimer particles containing splice insert A density.

Model building and refinement

Monomeric Ten3-A_0B_0 (6FAY, Jackson et al, 2018) was combined with models predicted by ColabFold[48] for EGF6-8 (A_0), C-rich, ABD, and Tox-GHH domains. Non-compact subunit models for the other isoforms were created by predicting structures for the EGF6-8 containing splice insert A, and NHL containing B, and substituting them in the initial A_0B_0 model. The Ten3 'stalk' was predicted by ColabFold multimer for a dimeric amino acid input spanning the residues of the ECD through EGF5, which exclusively resulted in stalks with EGF2-2/EGF5-5 configuration. To model the compact dimer, two A_1B_1 subunit models were refined in the compact dimer closed conformation full map by iterative cycles of real space refinement in phenix.real_space_refine of the Phenix package[49] and manual real-space refinement in Coot[50]. EGF6-7 and A that were outside the map were removed from the model. Residues and side chains lacking sufficient density were removed from the model to enhance the refinement process. At the final stages, the model was refined in the full map of teneurin-3 A_1B_1 compact dimer using C2 symmetry constraints in Phenix. A single subunit A_0B_0 model containing EGF6 through the C-terminal Tox-GHH domain was refined in the map in which EGF6 and 7 were additionally resolved. Before refinement, this model's C-rich domain was substituted for the C-rich domain from the final refined A_1B_1 compact dimer model. The stereochemistry of the models was checked with MolProbity[51], the interfaces were analysed with the Protein Interfaces, Surfaces and Assemblies (PISA)

web server[52]. The structural figures of maps and models were generated with Chimera[53] and PyMOL (Schrodinger Molecular Graphics System, DeLano Scientific, San Carlos, CA).

Small-angle X-ray scattering

SAXS was performed at the European Synchrotron Radiation Facility B29 beamline, at 12.5 keV operating energy equipped with a Pilatus3 2M detector. Samples at approximately 1 mg/mL were diluted two-fold twice in series, and then 50 microliters of each was injected. Data were collected at 20°C over 10 frames, one frame per second, with a scattering vector range of 0.0456–5.15 nm^{-1}. Radiation damage was monitored and data frames were selected manually in the PRIMUS GUI[54], which was also used for frame averaging, buffer subtraction, Guinier modeling, and determining the pair-distance distribution P(r). Kratky analyses were performed according to Durand *et al.* (2010)[55]. In preparation for rigid-body fitting, complex glycan trees were built manually on glycosylation sites of the compact models in Coot[50]. A model for the N-terminal domains that could not be resolved by cryo-electron microscopy was generated in ColabFold[48]. These were then taken together, and short flexible linkers were introduced between domains, conserving the interfaces of the compact dimers, as well as the EGF2/EGF5 covalent dimerization interface, and fit to the datasets of each splice insert was optimised using CORAL[56]. The fit of each resulting model to each dataset was then calculated in CRYSOL[57], using 50 as "number of spherical harmonics" and allowing for constant subtraction. All programs were used as implemented in ATSAS 3.1.3[58].

Thermal stability assay

Thermal shift assay (TSA) assays were performed using purified human Ten3 isoforms at a concentration of 0.5 mg/mL. Prior to the experiments, the samples were buffer exchanged into SEC buffer (150-mM NaCl, 20- mM HEPES, pH 7.8) without additional calcium denoted "SEC" condition, into SEC buffer supplemented with 2 mM $CaCl_2$ (physiological calcium) denoted "Ca^{2+}" condition, or into SEC buffer supplemented with 5 mM EDTA (no calcium) denoted "EDTA" condition. SYPRO Orange Dye (Invitrogen) was diluted to a concentration of 5X concentrated solution and filtered using a 0.22 μm membrane. Final protein concentrations were 60 μg/mL protein, 1× dye and final buffer concentrations 132 mM NaCl, 17.6 mM HEPES, pH 7.8, supplemented with 1.76 mM $CaCl_2$ or EDTA. A temperature ramp from 5°C to 95°C was set up at a speed of 0.02°C/s on a QuantStudio 3 Real-Time PCR system (Thermo Fisher Scientific). All measurements were performed in triplicates. The melting temperatures T_m were determined as the intersection of the x-axis with the smoothened second derivative of the melting curve between the valley and peak shown in the raw melting curves.

Negative stain imaging and analysis

Purified protein samples were diluted to 20 μg/mL before depositing 3.5 μL of the resulting sample volume onto glow-discharged carbon-coated copper grids for 2 min incubation. Excess sample volume was then blotted away, followed by three washing cycles of depositing 10 μL of SEC buffer supplemented with 2 mM $CaCl_2$ with subsequent blotting. The grid was then incubated with 3.5 μL 2% uranyl acetate or 1% uranyl formate (for A_0B_0) for another 60 sec before blotting the excess away. Grids were left to dry at RT for up to 2 min before imaging or storage. At least 20 micrographs were acquired for each sample using a JEOL JEM-1400Plus transmission electron microscope operating at 120 kV with a standard magnification of 30,000x, 1000 ms exposure, and a defocus value of -2.4 μm (or, Tecnai12 microscope operated at 120 kV for A_0B_0). Micrographs were processed using RELION3.1[44] before following standard reconstruction workflow. In short, particles were first picked using RELION's own Laplacian-of-Gaussian implementation, followed by reference-based particle picking after 2D classification. An initial 3D model was generated for multiple rounds of 3D classification of all particles. The final selection was refined and postprocessed in RELION.

Cell clustering assay

Cell electroporation for the clustering assays was performed as previously reported[59]. K562 cells (DSMZ) were cultured in RPMI-1640 medium (Gibco), supplemented with 10% FBS (Gibco) and 1% Penicillin/Streptomycin (Gibco), and grown in a shaking incubator at 37 °C and 5% CO_2. Prior to electroporation, K562 cells were centrifuged for 5 min at 300 g and washed in 1x PBS (Gibco). Cells were once again centrifuged for 5 min at 300 ×g and resuspended in buffer R (Gibco). Per condition, 2×10^6 cells were incubated with a total amount of 15 µg of DNA (Ten3:empty vector ratio was 1:5) for 15 min at room temperature. After the incubation, K562 cells were electroporated with the Neon Transfection System (Thermo Fisher Scientific), using the following parameters: 1450 V, 10 ms pulse length, and 3 pulses[7]. After electroporation, cells were directly seeded onto 5 mL of pre-warmed RPMI-1640 medium with 10% FBS in 6-well plates. Cells were placed in a shaking incubator at 37 °C and 5% CO2 for approximately 20 hours. Cells were imaged on an EVOS M5000 microscope with a 10x objective (0.25 NA; EVOS, Thermo Fisher Scientific), using the EVOS LED GFP cube (Thermo Fisher Scientific). The researcher was blind to which condition was being imaged to prevent bias for cluster formation. In the GFP channel, regions of interest (ROIs) larger than 100 pixels were identified using Fiji[60] Analyze Particles after rolling ball background subtraction with 50-pixel radius was performed. The area of each ROI was then measured. A cell cluster was defined as an object three times larger than the mean large single cell size (800 pixels). The clustering index was determined as the summed cluster area

divided by summed area of all ROIs (clusters + non-clusters) times 100%. The cluster size and clustering index were averaged per image, and data from three independent experiments (5 images per experiment, 15 images total per condition). Statistical significance was determined by performing a one-way ANOVA followed by a Tukey's multiple comparison test. All analysed data are represented as mean ± SEM.

Animals for neuronal assays

Fertilised chicken eggs (Gallus gallus, white leghorn) were obtained from a commercial dealer and incubated in a forced draft incubator at 37°C and 65% humidity until the desired embryonic stage.

In Situ Hybridisation (ISH)

Eyes from chick embryos at developmental day (E) 6 were fixed in 4% paraformaldehyde (PFA) solution for 2 days, followed by perfusion with 4% sucrose/ 0.5% PFA solution, until samples sunk to the bottom of the tube. Eyes were embedded in O.C.T. cryo-embedding matrix prior to cryo-sectioning. 20μm-thick coronal sections were cut on the cryostat to obtain dorsoventral sections of the chick retina and stored at -80°C. Sections were rehydrated for 5 min in PBS-T (1x PBS + 0.1% Tween-20), and permeabilised by digestion with 5μg/mL Proteinase K for 5 min at room temperature. Digestion was inhibited by 2mg/mL (2%) glycine in PBS-T, followed by 2 times 5 min washes with PBS-T and fixation with 4% PFA for 20 min. Residual PFA was removed by washing twice with PBS-T for 5 min, and sections were prehybridised in hybridisation mix (50% formamide, 5x SSC pH 4.5, 50μg/mL tRNA, 1% SDS and 50μg/mL Heparin) for 1 hour at 65°C, prior to hybridisation of probe overnight at 65°C. Sections were washed 3 times for 15 min with a solution containing 50% formamide, 5 X SSC pH 4.5 and 1% SDS and 3 times for 15 min in solution comprising 50% formamide, 2 X SSC pH 4.5, at 65°C and 60°C, respectively.

After blocking for 1 hour at room temperature with 10% sheep serum in TBS-T (1x TBS + 0.1% Tween-20), sections were incubated with Alkaline Phosphatase (AP)-conjugated anti-DIG antibody (Roche) diluted 1:2000 in 10% sheep serum in TBS-T overnight at 4°C. Samples were extensively washed to remove excess antibody. Sections were then washed thrice for 10 min in NTMT buffer containing 100mM NaCl, 100mM Tris-HCl pH 9.5, 100mM MgCl2 and 1% Tween-20. The colour staining was developed at room temperature and in the dark using NBT/BCIP stock solution (75mg/mL and 50mg/mL, respectively) (Roche) diluted 1:200 in NTMT buffer. The reaction was terminated by 2 washes for 10 min in NTMT, followed by a wash in PBS-T pH 5.5 for 10 min and 2 washed for 10 min in 1x PBS. Samples were postfixed in 4% PFA in PBS for 30 min at room temperature and stained with Hoechst diluted 1:10,000 in 1x TBS before a final wash in PBS and mounting in 90% glycerol.

Stripe assays

Stripe assays were performed according to a previously established protocol[61]. Prior to the experiment, specially designed silicone matrices were boiled in autoclaved water, glass coverslips were coated in 10µg/mL poly-L-lysine (PLL) for 1 hour and both were left to dry overnight in a laminar flow hood. On the day of the experiment, dry matrices were fixed onto glass coverslips and rinsed with ethanol and Hank's Basic Salt Solution (HBSS) using a Hamilton syringe. Ten3-B_0/B_1 monomeric (referred to as Ten3 from now on) proteins were diluted in HBSS (ThermoFisher) and used at a concentration of 10µg/mL in final stripe assays. Ten3 was clustered using anti-6xHis Tag antibodies (GeneTex) and fluorescently labelled using a goat anti-rabbit AlexaFluor 568 secondary antibody (ThermoFisher). The anti-6xHis Tag antibody (10µg/mL) alone was used for generating control stripes (second stripe). Laminin and merosin solutions were prepared to final concentrations of 5µg/µL and 1µg/mL, respectively by combining equal volumes of both solutions. Neurobasal (NB) medium was supplemented with 2% methylcellulose, 1% B27, 1% glutamine, 1% Penicillin / Streptomycin (Pen/Strep) and 0.01% forskolin.

To generate the first set of stripes, purified protein solutions were injected into the matrices using a Hamilton syringe and culture dishes were incubated at 37°C/ 5% CO_2 for 45 min. Following the removal of matrices from the coverslips and HBSS wash, unlabelled second stripe solution, containing the anti-6xHis Tag antibody in HBSS, was pipetted on top of the stripes. Culture dishes were incubated for 45 min at 37°C and coverslips subsequently coated with laminin/merosin solution for 1 hour. Freshly dissected chick retinas at embryonic stage E6 were flat-mounted on nitrocellulose filter paper and cut into ~2mm wide strips along the dorsoventral axis using a tissue chopper. Explant strips were placed on top of protein stripes and incubated at 37°C/ 5%CO2 for up to three days in neurobasal media. Explant strips were fixed in 4% PFA/ 0.33% sucrose for 15-20 min at room temperature and permeabilised by washing twice for 5 min with 1x PBS/0.1%Triton and subsequently stained by incubation with 1:200 phalloidin conjugated with- AlexaFluor 488 for 20 min at room temperature, in a wet chamber and under aluminium foil. After a series of washes to remove excess staining solution, coverslips were mounted onto glass slides using Mowiol. Stripe assays were imaged using a Fluorescence microscope (Zeiss) at 20x magnification. Three independent rounds of stripe assays were performed, each round consisting of 4-6 individual assays per condition (Control vs Ten3), using explants from at least 2 animals. For individual stripe assay, two images were taken from the ventral and dorsal regions of each retinal explant strip. Axon guidance decisions in all images were scored blindly by 3 people, in accordance with a previously established scoring system, with values between -3, 0 and +3, representing strong repulsion, no guidance and strong attraction, respectively[61,62]. Mean scores were calculated and plotted using GraphPad (mean ±

SEM), and statistical significance was determined with Two-way ANOVA with Tukey's multiple comparisons tests.

References

1. Tucker RP, Beckmann J, Leachman NT, Schöler J, Chiquet-Ehrismann R. Phylogenetic analysis of the teneurins: Conserved features and premetazoan ancestry. *Mol Biol Evol*. 2012;29(3):1019-1029. doi:10.1093/molbev/msr271

2. Zhou XH, Brandau O, Feng K, et al. The murine Ten-m/Odz genes show distinct but overlapping expression patterns during development and in adult brain. *Gene Expression Patterns*. 2003;3(4):397-405. doi:10.1016/S1567-133X(03)00087-5

3. Cheung A, Trevers KE, Reyes-Corral M, Antinucci P, Hindges R. Expression and Roles of Teneurins in Zebrafish. *Front Neurosci*. 2019;13. doi:10.3389/fnins.2019.00158

4. Beckmann J, Schubert R, Chiquet-Ehrismann R, Müller DJ. Deciphering teneurin domains that facilitate cellular recognition, cell-cell adhesion, and neurite outgrowth using atomic force microscopy-based single-cell force spectroscopy. *Nano Lett*. 2013;13(6):2937-2946. doi:10.1021/nl4013248

5. Meijer DH, Frias CP, Beugelink JW, Deurloo YN, Janssen BJC. Teneurin4 dimer structures reveal a calcium-stabilized compact conformation supporting homomeric trans-interactions. *EMBO J*. 2022;41(9). doi:10.15252/embj.2020107505

6. Sando R, Jiang X, Südhof TC. Latrophilin GPCRs direct synapse specificity by coincident binding of FLRTs and teneurins. *Science (1979)*. 2019;363(6429). doi:10.1126/science.aav7969

7. Pederick DT, Lui JH, Gingrich EC, et al. Reciprocal repulsions instruct the precise assembly of parallel hippocampal networks. Science. 2021; 372(6546):1068-1073. doi:10.1126/science.abg1774

8. Cheung A, Schachermayer G, Biehler A, Wallis A, Missaire M, Hindges R. Teneurin paralogues are able to localise synaptic sites driven by the intracellular domain and have the potential to form cis-heterodimers. *Front Neurosci*. 2022;16. doi:10.3389/fnins.2022.915149

9. Boucard AA, Maxeiner S, Südhof TC. Latrophilins function as heterophilic cell-adhesion molecules by binding to teneurins: Regulation by alternative splicing. *Journal of Biological Chemistry*. 2014;289(1):387-402. doi:10.1074/jbc.M113.504779

10. Berns DS, DeNardo LA, Pederick DT, Luo L. Teneurin-3 controls topographic circuit assembly in the hippocampus. *Nature*. 2018;554(7692):328-333. doi:10.1038/nature25463

11. del Toro D, Carrasquero-Ordaz MA, Chu A, et al. Structural Basis of Teneurin-Latrophilin Interaction in Repulsive Guidance of Migrating Neurons. *Cell*. 2020;180(2):323-339.e19. doi:10.1016/j.cell.2019.12.014

12. Spead O, Moreland T, Weaver CJ, et al. Teneurin trans-axonal signaling prunes topographically missorted axons. *Cell Rep*. 2023;42(3). doi:10.1016/j.celrep.2023.112192

13. Mosca TJ. On the Teneurin track: A new synaptic organization molecule emerges. *Front Cell Neurosci*. 2015;9(MAY). doi:10.3389/fncel.2015.00204

14. Yuen RKC, Thiruvahindrapuram B, Merico D, et al. Whole-genome sequencing of quartet families with autism spectrum disorder. *Nat Med*. 2015;21(2):185-191. doi:10.1038/nm.3792

15. Singh B, Srivastava P, Phadke SR. Sequence variations in TENM3 gene causing eye anomalies with intellectual disability: Expanding the phenotypic spectrum. *Eur J Med Genet*. 2019;62(1):61-64. doi:10.1016/j.ejmg.2018.05.004

16. Burbach PPH, Meijer DH. Latrophilin's social protein network. *Front Neurosci*. 2019;13(JUN). doi:10.3389/fnins.2019.00643

17. Jackson VA, Meijer DH, Carrasquero M, et al. Structures of Teneurin adhesion receptors reveal an ancient fold for cell-cell interaction. *Nat Commun*. 2018;9(1). doi:10.1038/s41467-018-03460-0

18. Li J, Shalev-Benami M, Sando R, et al. Structural Basis for Teneurin Function in Circuit-Wiring: A Toxin Motif at the Synapse. *Cell*. 2018;173(3):735-748.e15. doi:10.1016/j.cell.2018.03.036

19. Dodsworth TL, Lovejoy DA. Role of Teneurin C-Terminal Associated Peptides (TCAP) on Intercellular Adhesion and Communication. *Front Neurosci*. 2022;16. doi:10.3389/fnins.2022.868541

20. Oohashi T, Zhou XH, Feng K, et al. *Mouse Ten-m/Odz Is a New Family of Dimeric Type II Transmembrane Proteins Expressed in Many Tissues*. Vol 145.; 1999. http://www.jcb.org

21. Feng K, Zhou XH, Oohashi T, et al. All four members of the Ten-m/Odz family of transmembrane proteins form dimers. *Journal of Biological Chemistry*. 2002;277(29):26128-26135. doi:10.1074/jbc.M203722200

22. Li J, Bandekar SJ, Araç D. The structure of fly Teneurin-m reveals an asymmetric self-assembly that allows expansion into zippers. *EMBO Rep*. 2023;24(6). doi:10.15252/embr.202256728

23. Li J, Xie Y, Cornelius S, et al. Alternative splicing controls teneurin-latrophilin interaction and synapse specificity by a shape-shifting mechanism. *Nat Commun*. 2020;11(1). doi:10.1038/s41467-020-16029-7

24. Meijers R, Puettmann-Holgado R, Skiniotis G, et al. Structural basis of Dscam isoform specificity. *Nature*. 2007;449(7161):487-491. doi:10.1038/nature06147

25. Sawaya MR, Wojtowicz WM, Andre I, et al. A Double S Shape Provides the Structural Basis for the Extraordinary Binding Specificity of Dscam Isoforms. *Cell*. 2008;134(6):1007-1018. doi:10.1016/j.cell.2008.07.042

26. Li SA, Cheng L, Yu Y, Wang JH, Chen Q. Structural basis of Dscam1 homodimerization: Insights into context constraint for protein recognition. *Sci Adv*. 2016;2(5). doi:10.1126/sciadv.1501118

27. Cheng J, Yu Y, Wang X, et al. Structural basis for the self-recognition of sDSCAM in Chelicerata. *Nat Commun*. 2023;14(1). doi:10.1038/s41467-023-38205-1

28. Um JW, Kim KH, Park BS, et al. Structural basis for LAR-RPTP/Slitrk complex-mediated synaptic adhesion. *Nat Commun*. 2014;5. doi:10.1038/ncomms6423

29. Yamagata A, Sato Y, Goto-Ito S, et al. Structure of Slitrk2-PTP complex reveals mechanisms for splicing-dependent trans-synaptic adhesion. *Sci Rep*. 2015;5. doi:10.1038/srep09686

30. Lin Z, Liu J, Ding H, Xu F, Liu H. Structural basis of SALM5-induced PTPδ dimerization for synaptic differentiation. *Nat Commun*. 2018;9(1). doi:10.1038/s41467-017-02414-2

31. Araç D, Boucard AA, Özkan E, et al. Structures of Neuroligin-1 and the Neuroligin-1/Neurexin-1β Complex Reveal Specific Protein-Protein and Protein-Ca2+ Interactions. *Neuron*. 2007;56(6):992-1003. doi:10.1016/j.neuron.2007.12.002

32. Wilson SC, White KI, Zhou Q, et al. Structures of neurexophilin–neurexin complexes reveal a regulatory mechanism of alternative splicing. *EMBO J*. 2019;38(22). doi:10.15252/embj.2019101603

33. Yamagata A, Yoshida T, Sato Y, et al. Mechanisms of splicing-dependent trans-synaptic adhesion by PTPδ -IL1RAPL1/IL-1RAcP for synaptic differentiation. *Nat Commun*. 2015;6. doi:10.1038/ncomms7926

34. Furlanis E, Scheiffele P. Regulation of Neuronal Differentiation, Function, and Plasticity by Alternative Splicing. *Annu Rev Cell Dev Biol*. 2018;34(July):451-469. doi:10.1146/annurev-cellbio-100617-062826

35. Suzuki S, Ayukawa N, Okada C, et al. Spatio-temporal and dynamic regulation of neurofascin alternative splicing in mouse cerebellar neurons. *Sci Rep*. 2017;7(1):1-13. doi:10.1038/s41598-017-11319-5

36. Chih B, Gollan L, Scheiffele P. Alternative Splicing Controls Selective Trans-Synaptic Interactions of the Neuroligin-Neurexin Complex. *Neuron*. 2006;51(2):171-178. doi:10.1016/j.neuron.2006.06.005

37. Li Y, Zhang P, Choi TY, et al. Splicing-Dependent Trans-synaptic SALM3-LAR-RPTP Interactions Regulate Excitatory Synapse Development and Locomotion. *Cell Rep*. 2015;12(10):1618-1630. doi:10.1016/j.celrep.2015.08.002

38. Karki S, Shkumatov A V., Bae S, Kim H, Ko J, Kajander T. Structural basis of SALM3 dimerization and synaptic adhesion complex formation with PTPσ. *Sci Rep*. 2020;10(1). doi:10.1038/s41598-020-68502-4

39. Coles CH, Mitakidis N, Zhang P, et al. Structural basis for extracellular cis and trans RPTPσ signal competition in synaptogenesis. *Nat Commun*. 2014;5. doi:10.1038/ncomms6209

40. Wojtowicz WM, Wu W, Andre I, Qian B, Baker D, Zipursky SL. A Vast Repertoire of Dscam Binding Specificities Arises from Modular Interactions of Variable Ig Domains. *Cell*. 2007;130(6):1134-1145. doi:10.1016/j.cell.2007.08.026

41. Biederer T, Kaeser PS, Blanpied TA. Transcellular Nanoalignment of Synaptic Function. *Neuron*. 2017;96(3):680-696. doi:10.1016/j.neuron.2017.10.006

42. Trotter JH, Hao J, Maxeiner S, et al. Synaptic neurexin-1 assembles into dynamically regulated active zone nanoclusters. *Journal of Cell Biology*. 2019;218(8):2677-2698. doi:10.1083/JCB.201812076

43. Zhang X, Lin PY, Liakath-Ali K, Südhof TC. Teneurins assemble into presynaptic nanoclusters that promote synapse formation via postsynaptic non-teneurin ligands. *Nat Commun*. 2022;13(1). doi:10.1038/s41467-022-29751-1

44. Scheres SHW. RELION: Implementation of a Bayesian approach to cryo-EM structure determination. *J Struct Biol*. 2012;180(3):519-530. doi:10.1016/j.jsb.2012.09.006

45. Zheng SQ, Palovcak E, Armache JP, Verba KA, Cheng Y, Agard DA. MotionCor2: Anisotropic correction of beam-induced motion for improved cryo-electron microscopy. *Nat Methods*. 2017;14(4):331-332. doi:10.1038/nmeth.4193

46. Zhang K. Gctf: Real-time CTF determination and correction. *J Struct Biol*. 2016;193(1):1-12. doi:10.1016/j.jsb.2015.11.003

47. Punjani A, Rubinstein JL, Fleet DJ, Brubaker MA. CryoSPARC: Algorithms for rapid unsupervised cryo-EM structure determination. *Nat Methods*. 2017;14(3):290-296. doi:10.1038/nmeth.4169

48. Mirdita M, Schütze K, Moriwaki Y, Heo L, Ovchinnikov S, Steinegger M. ColabFold: making protein folding accessible to all. *Nat Methods*. 2022;19(6):679-682. doi:10.1038/s41592-022-01488-1

49. Adams PD, Afonine P V., Bunkóczi G, et al. PHENIX: A comprehensive Python-based system for macromolecular structure solution. *Acta Crystallogr D Biol Crystallogr*. 2010;66(2):213-221. doi:10.1107/S0907444909052925

50. Emsley P, Cowtan K. Coot: Model-building tools for molecular graphics. *Acta Crystallogr D Biol Crystallogr*. 2004;60(12 I):2126-2132. doi:10.1107/S0907444904019158

51. Williams CJ, Headd JJ, Moriarty NW, et al. MolProbity: More and better reference data for improved all-atom structure validation. *Protein Science*. 2018;27(1):293-315. doi:10.1002/pro.3330

52. Krissinel E, Henrick K. Inference of Macromolecular Assemblies from Crystalline State. *J Mol Biol*. 2007;372(3):774-797. doi:10.1016/j.jmb.2007.05.022

53. Pettersen EF, Goddard TD, Huang CC, et al. UCSF ChimeraX: Structure visualization for researchers, educators, and developers. *Protein Science*. 2021;30(1):70-82. doi:10.1002/pro.3943

54. Konarev P V., Volkov V V., Sokolova A V., Koch MHJ, Svergun DI. PRIMUS: A Windows PC-based system for small-angle scattering data analysis. *J Appl Crystallogr*. 2003;36(5):1277-1282. doi:10.1107/S0021889803012779

55. Durand D, Vivès C, Cannella D, et al. NADPH oxidase activator p67phox behaves in solution as a multidomain protein with semi-flexible linkers. *J Struct Biol*. 2010;169(1):45-53. doi:10.1016/j.jsb.2009.08.009

56. Petoukhov M V., Franke D, Shkumatov A V., et al. New developments in the ATSAS program package for small-angle scattering data analysis. *J Appl Crystallogr*. 2012;45(2):342-350. doi:10.1107/S0021889812007662

57. Svergun D, Barberato C, Koch MHJ. *CRYSOL-a Program to Evaluate X-Ray Solution Scattering of Biological Macromolecules from Atomic Coordinates*. Vol 28.; 1995.

58. Manalastas-Cantos K, Konarev P V., Hajizadeh NR, et al. ATSAS 3.0: Expanded functionality and new tools for small-angle scattering data analysis. *J Appl Crystallogr*. 2021;54:343-355. doi:10.1107/S1600576720013412

59. Chataigner LMP, Gogou C, den Boer MA, et al. Structural insights into the contactin 1 – neurofascin 155 adhesion complex. *Nat Commun*. 2022;13(1). doi:10.1038/s41467-022-34302-9

60. Schindelin J, Arganda-Carreras I, Frise E, et al. Fiji: An open-source platform for biological-image analysis. *Nat Methods*. 2012;9(7):676-682. doi:10.1038/nmeth.2019

61. Knöll B, Weinl C, Nordheim A, Bonhoeffer F. Stripe assay to examine axonal guidance and cell migration. *Nat Protoc*. 2007;2(5):1216-1224. doi:10.1038/nprot.2007.157

62. Walter J, Kern-Veits B, Huf J, Stolze B, Bonhoeffer F. *Recognition of Position-Specific Properties of Tectai Cell Membranes by Retinal Axons in Vitro*. Vol 101.; 1987.

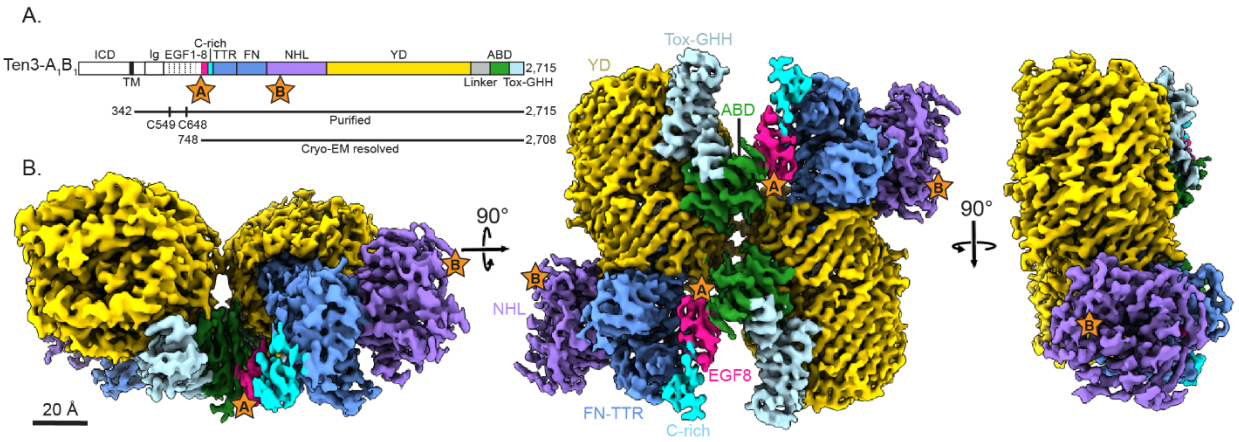

Figure 1: Teneurin-3 A_1B_1 core superfolds form a compact dimer. **A)** Linear representations of the full-length teneurin-3 A_1B_1 domain composition. Splice insert are indicated as stars: splice insert A in between EGF7 and EGF8; splice insert B in the NHL domain. The expressed and purified ectodomain is indicated with the black line below. Free cystines in EGF2 (C549) and EGF5 (C648) that enable constitutive dimerization are indicated. The bottom black line indicates domains resolved using cryo-EM (EGF8 through Tox-GHH). ICD, intracellular domain; Ig, immunoglobulin fold; EGF, epidermal growth factor repeat domains 1 through 8; C-rich, cysteine-rich region; TTR, transthyretin-related; FN, fibronectin plug; NHL, NCL, HT2A and Lin-41; YD, tyrosine-aspartate; ABD, antibiotic-binding domain; Tox-GHH, toxin-glycine-histidine-histidine. **B)** Three different views of the density map

of the teneurin-3 A_1B_1 compact dimer at 3.3 Å resolution. Domain annotations are coloured corresponding to the linear representation in A). Positions of the splice sites are indicated with stars. Scale bar is 20 Å.

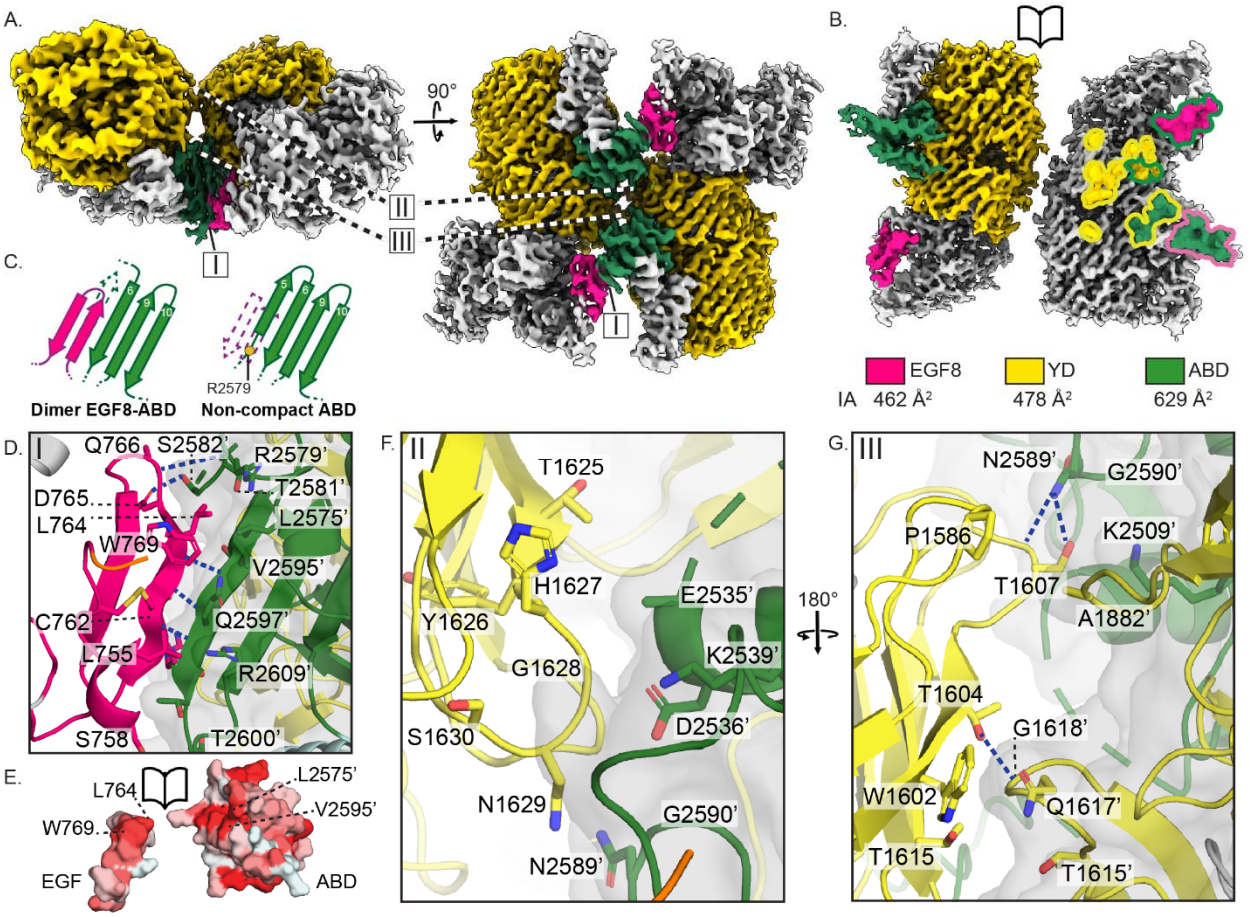

Figure 2: The teneurin-3 A_1B_1 compact dimer interface comprises three distinct interaction sites. **A)** Density map of the Ten3-A_1B_1 compact dimer with domains that participate in the interfaces shown in colour. Colour code is shown below panels B, along with the interface area (IA) per domain. **B)** Open book representation of the electron density. The left subunit shows the participating domain in colour, and the right subunit displays the specific interface residues. Fill colours indicate the domains in which the residues are located, and outline colours indicate the domains in which the contacting residues reside. **C)** Schematic representation of EGF8-ABD interface in the compact dimer versus the ABD domain of a Ten3 A_1B_1 non-compact subunit reconstruction. Residues 2588-2599 are displaced or disordered in the compact dimer form and residues 2582-2587 form β-strand 5 in ABD of the non-compact subunit. **D)** Close-up of interface I, the EGF8-ABD extended β-sheet. For clarity, only residues that contribute directly to the interface, or demarcate boundaries of stretches of interface residues are labelled. **E)** Open book surface hydrophobicity representation of the EGF8-ABD interface. **F)** Close-up of interface II, comprising YD-ABD contacts. **G)** Close-up of interface III, the YD-YD and YD-ABD contacts. In the close-ups, hydrogen bonds are indicated in dashed blue lines, and transparent surface representation is used to distinguish between subunits within the compact dimer. Only residues with >5% per-residue buried surface area are represented.

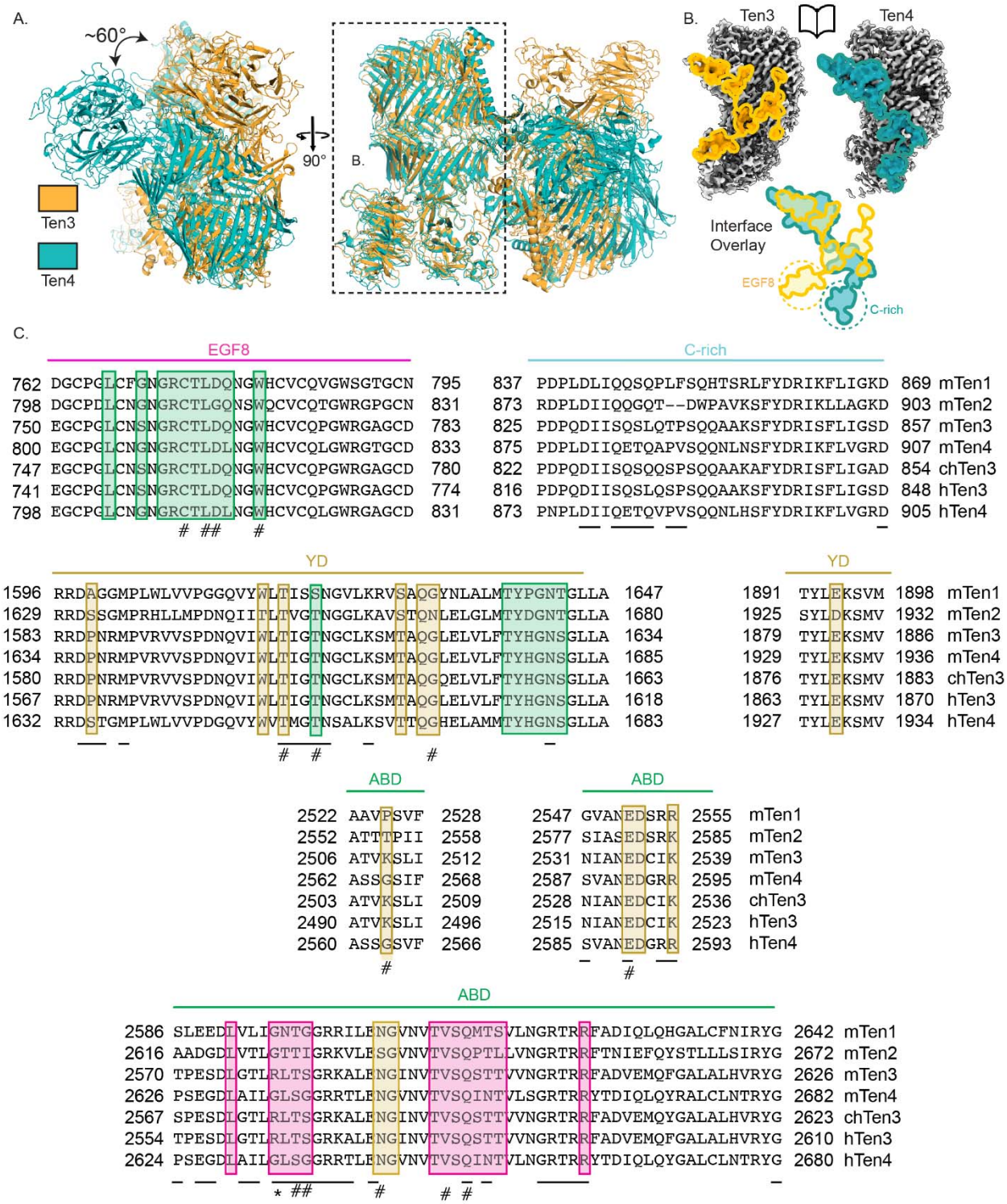

Figure 3: Teneurin-3 and teneurin-4 (Ten4) compact dimer interfaces are different. **A)** Alignment of one subunit from the teneurin-3 (Ten3) compact dimer conformation with one subunit from the teneurin-4 (Ten4) dimer. The remaining subunits from each dimer orient at a relative angle of approximately 60°. Dashed outline indicates the subunit represented in panel B. **B)** Comparison of the mouse Ten3 and human Ten4 compact dimer interface

projections on open-book subunits. Below: overlays of the interface projections. Dashed circles indicate the domains that exclusively participate in one or the other compact dimer. **C)** Teneurin alignment across orthologues of the interface residues for the EGF8, C-rich, YD and ABD domains. Boxes around the residues indicate the contacting domains in mouse teneurin-3. Domain colouring corresponds to that in Fig. 1. Only residues with >5% per-residue buried surface area are represented. #, hydrogen-bonding residues in Ten3; _, interface residues in Ten4; *, Arg2579, the mouse homologue of microphthalmia-associated Arg2563 in humans.

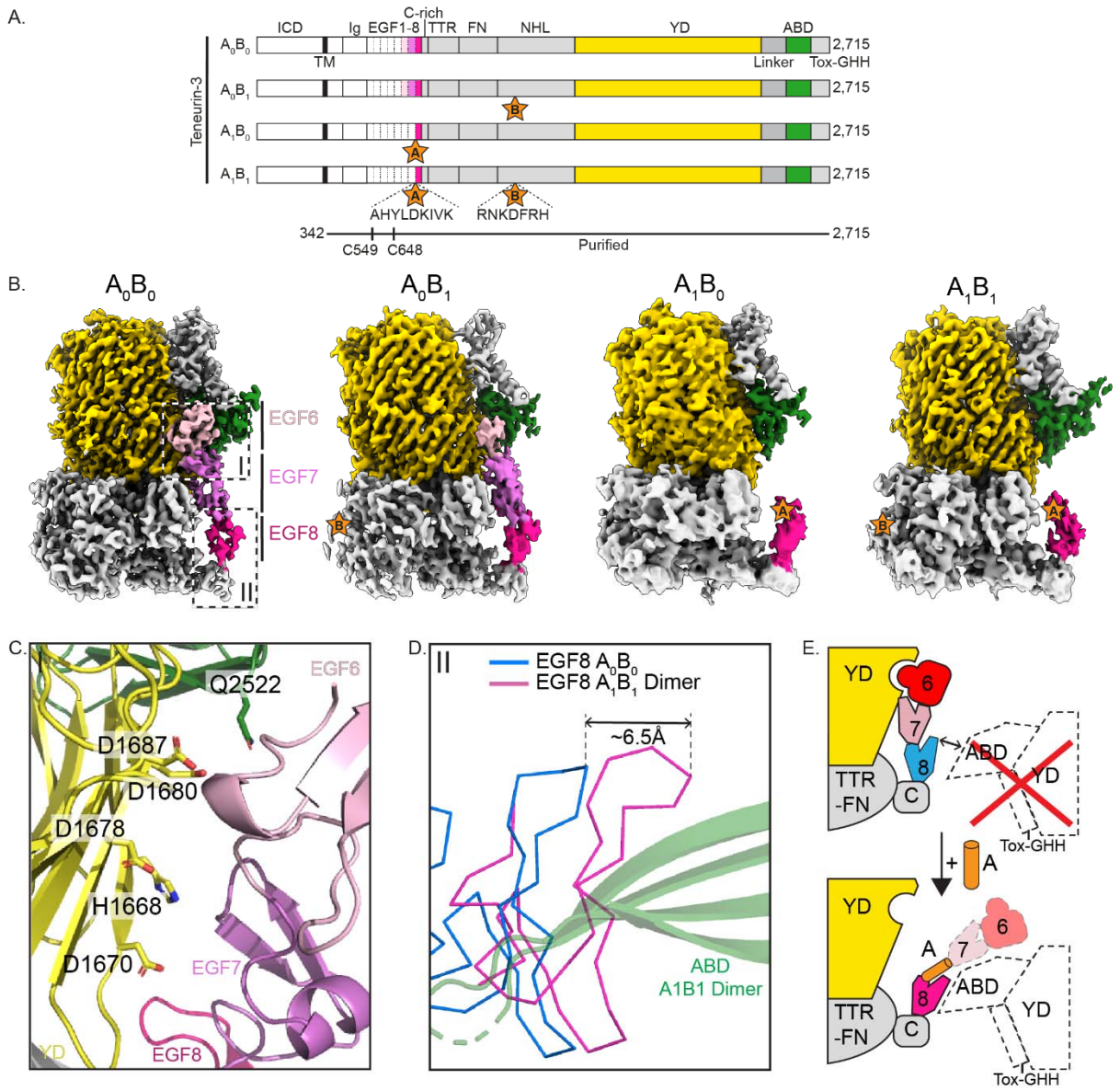

Figure 4: Subunits of A_0 isoforms display a contact between EGF6 and the YD, ABD domains. **A)** Linear representations of the four full-length Ten3 isoforms with domain composition. Presence of splice inserts indicated with stars. Domains are labelled according to Fig. 1. **B)** Cryo-EM reconstructions of isoform subunits. Dashed boxes I.-II. indicate close-ups shown in panels C-D, respectively. **C)** EGF6-YD/ABD interface. Interacting residues on the YD- and ABD-side of the interface are displayed and annotated. **D)** Overlay of EGF8 domains of Ten3-A_0B_0 and A_1B_1. The relative displacement of EGF8 is indicated. **E)** Schematic representation of dislodging by splice insert A. Top: Absence of A is accompanied by an additional interface between EGF6-YD/ABD. This stabilisation impedes EGF8 β-sheet extension with ABD for compact dimerisation. Below: Splice insert A creates distance between EGF7 and EGF8, in turn dislodging the EGF6-YD interface. Loss of this interface and the presence of splice insert A increases the flexibility of the EGF region and EGF8 is now free to interact with the opposite ABD domain.

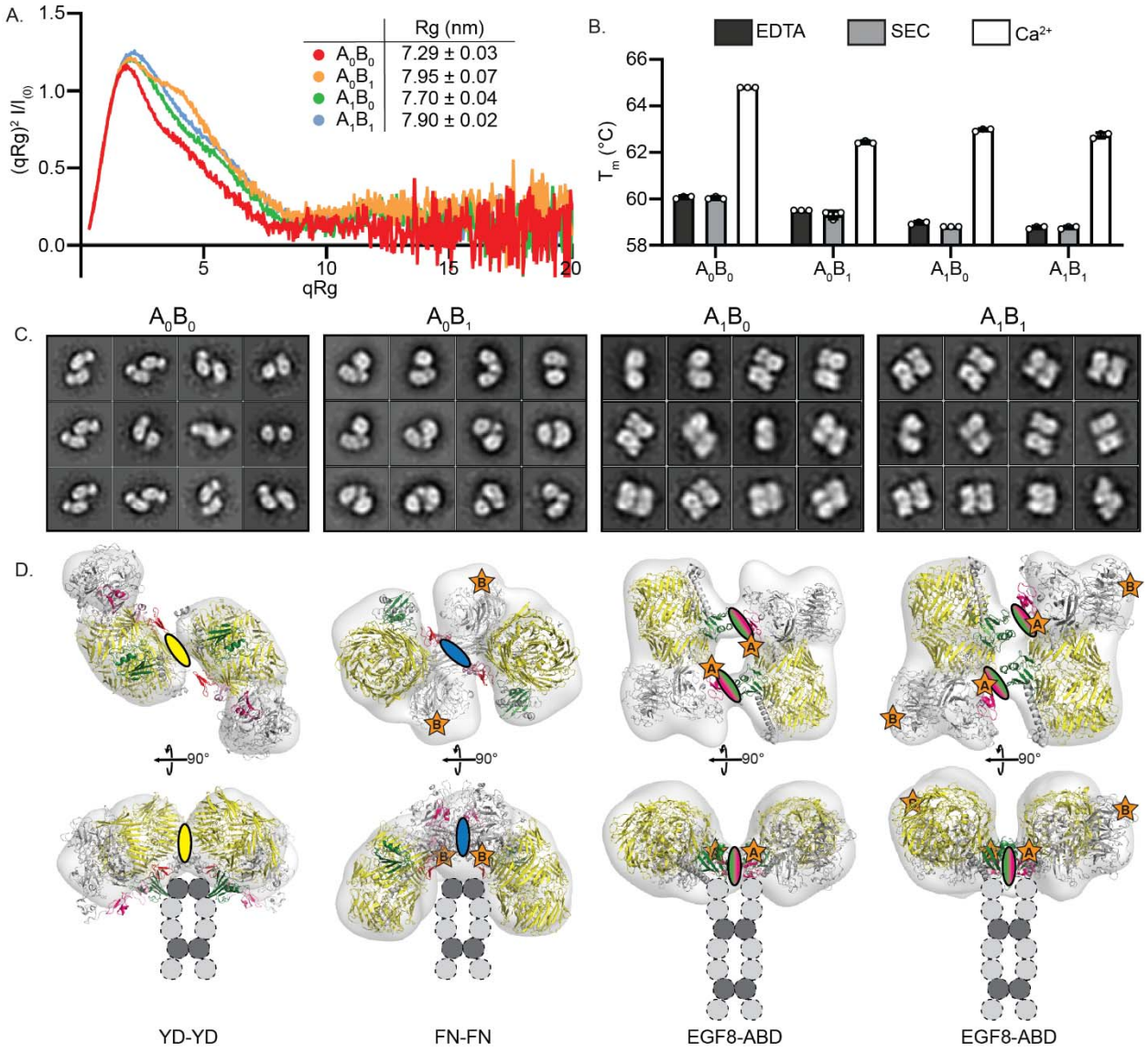

Figure 5: All teneurin-3 isoforms are compact in solution with isoform-specific conformations. **A)** Dimensionless Kratky-plot of SAXS data for all Ten3 isoforms at 0.5 mg/mL in the presence of 2 mM Ca^{2+}. Inset, radii of gyration (mean ± SEM) derived from SAXS data for each isoform in the absence (SEC) and presence of 2 mM Ca^{2+} (Ca^{2+}) versus the presence of 5 mM EDTA (EDTA). **B)** Melting temperatures (T_m) for each isoform for the conditions as in A. Single datapoints in B-C represent SAXS measurements repeats at Ten3 concentration of 1.0, 0.5, and 0.25 mg/mL. **C)** 2D classes of negative stain TEM for all Ten3 isoforms. **D)** 3D reconstructions for all splice variants, shown at two different angles. Ovals indicate location of the compact dimer interface, and the colour denotes the involved domain(s) according to domain colouring in Fig. 1. Attachment of the EGF repeats that are not included in the map or model are added schematically as dashed circles. Disulphide-linked EGFs 2 and 5 shown in dark grey.

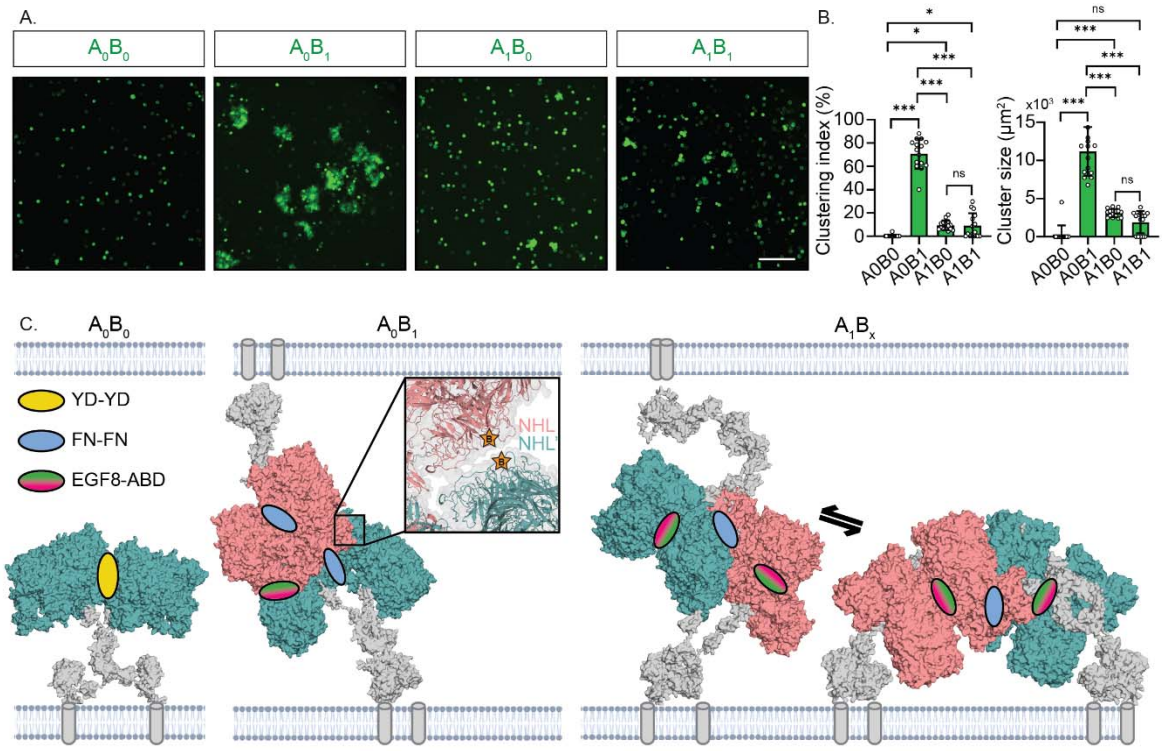

Figure 6: Models for teneurin-3 homophilic *trans*-cellular complex formation. **A)** Clustering assay of K562 hematopoietic cells electroporated with the mouse Ten3 isoforms. Scale bar is 100 µm. **B)** Analysis of the clustering indices and mean cluster area of the conditions in A. Data points correspond to the values of each image (5 images per N=3 independent experiments, 15 images total) - per-image average values for cluster size. Error bars indicate the mean ± SEM; ns: not significant, *: $p < 0.05$, ***: $p < 0.001$. One-Way ANOVA, Tukey's multiple comparisons test. **C)** A non-clustering Ten3-A_0B_0 compact dimer, a *trans*-cellular dimer-of-dimer of Ten3-A_0B_1, and a *trans*-cellular dimer-of-dimer of Ten3-A_1B_x. The A_0B_x dimer-of-dimers is also compatible with a *cis* configuration due to the EGF organisation. Close-up of the A_0B_1 *trans* dimer-of-dimers display an additional contact between the NHL domains of subunits not involved in the EGF8-ABD contact. Dimers located on opposing membranes are dinstinctly coloured salmon and dark teal. The rigid-body models of each of the EGF-Ig stalks were calculated using the SAXS data of each isoform (Fig. 5 and Supplemental Fig. 4G).

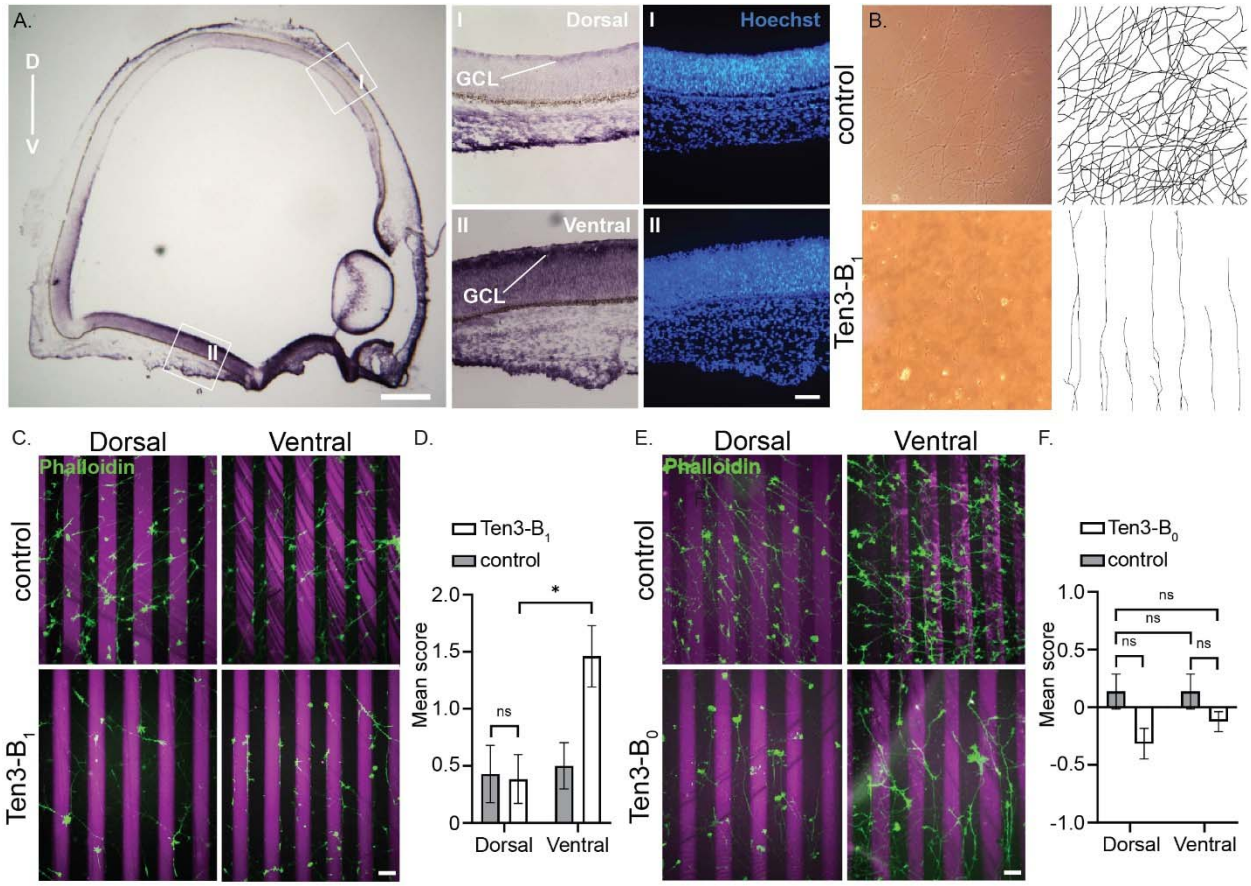

Figure 7: Splice insert B directly guides axons. **A)** In situ hybridisation on E6 chick retinal cryosections showing chick Ten3 mRNA expression in a gradient along dorso-ventral (D-V) axis. GCL= ganglion cell layer. Scale bar is 400 µm. I. Close up of dorsal (D) region of the retina showing little to no expression of Ten3, and Hoechst staining of nuclei (blue) in V retina. II. Close up of ventral (V) region of the retina showing high expression of Ten3, and Hoechst staining of nuclei (blue) in D retina. **B)** Light microscope image of V RGC axons cultured on control versus Ten3-B_1-covered stripes. Scale bar is 50 µm. Right: Tracing of axons in the light microscopy images. **C)** Control stripe assays with cultured retinal explants from D and V retinas. Stripes were labelled with goat anti-Rabbit Alexa-568 secondary antibody and RGC axons labelled with Phalloidin-Alexa Fluor 488. Scale bar is 100 µm. Ten3 stripe assays with 10 µg/mL Ten3-B_1 (magenta), with retinal explants from D and V retina. **D)** Quantification of axon guidance in panel E of RGC axons from V vs D retina in control and Ten3-B_1 assays. Guidance decisions were scored between -3, -2, -1, 0, 1, 2 or 3, reflecting varied degrees or repulsion or attraction; n= 16-22 assays per condition, from 3 separate rounds; ns: not significant, *: $p < 0.05$. Two-Way ANOVA, Tukey's multiple comparisons test. **E)** Control stripe assays with cultured retinal explants from D and V retinas. Stripes were labelled with goat anti-Rabbit Alexa-568 secondary antibody and RGC axons labelled with Phalloidin-Alexa Fluor 488. Scale bar is 100 µm. Ten3 stripe assays with 10 µg/mL Ten3-B_0 (magenta), with retinal explants from D and V retina. **F)** Quantification of axon guidance decisions in panel C of RGC axons from V vs D retina in control and Ten3-B_0 assays. Guidance decisions were scored between -3, -2, -1, 0, 1, 2 or 3, reflecting varied degrees or

repulsion or attraction; n=13-14 assays per condition, from 3 separate rounds; ns: not significant, *: $p < 0.05$. Two-Way ANOVA, Tukey's multiple comparisons test.